Bottom Crack Detection with Real-Time Signal Amplitude Correction Using EMAT-PEC Composite Sensor

Yizhou Guo , Yu Hu , Kai Wang , Yini Song , Bo Feng , Yihua Kang , Zhaoqi Duan *

Posted Date: 26 July 2024

doi: 10.20944/preprints202407.2152.v1

Keywords: bottom crack; lift-off; EMAT; PEC; amplitude correction; signal fusion

Article

Bottom Crack Detection with Real-Time Signal Amplitude Correction Using EMAT-PEC Composite Sensor

Yizhou Guo, Yu Hu, Kai Wang, Yini Song, Bo Feng, Yihua Kang and Zhaoqi Duan *

School of Mechanical Science and Engineering, Huazhong University of Science and Technology, Hubei 430074, China

* Correspondence: zqduan@ucla.edu

Abstract: In electromagnetic ultrasonic testing, it is difficult to recognize small-size bottom cracks by time of flight (ToF), and the lift-off fluctuation of the probe affects the accuracy and consistency of the inspection results. In order to overcome the difficulty, a novel EMAT (electromagnetic acoustic transducer)-PEC (pulse eddy current) composite sensor is designed. We use amplitude of bottom echo recorded by EMAT to identify the tiny bottom crack as well as the amplitude of PEC signals picked up by the integrated symmetric coils to measure the average lift-off of the probe in real time. Firstly, the effects of lift-off and bottom cracks on amplitude of bottom echo are distinguished combining the theoretical analysis and finite element method (FEM). And then an amplitude correction method based on the fusion of EMAT and PEC signals is proposed to reduce the impact of lift-off on the defect signal. The experimental results demonstrate that the designed composite sensor can effectively detect the bottom crack as small as 0.1mm* 0.3mm. The signal fusion method can accurately correct the amplitude of defect signal and the relative error is less than ±8%.

Keywords: bottom crack; lift-off; EMAT; PEC; amplitude correction; signal fusion

1. Introduction

Crack emergence and expansion are among critical factors that affect the performance and longevity of structural steel such as plates, pipelines, and so on [1,2]. Typically, the cracks usually start with the opening sizes of 0.05-0.40 mm and may develop to dangerous sizes of tens of millimeters [1]. Non-destructive testing (NDT) techniques are used to inspect materials without damaging the sample under detection [3]. In NDT fields, the common methods of surface cracks detection mainly include Magnetic Flux Leakage (MFL) [4–6], Eddy Current Testing (ECT) [7–9], which are only able to detect the cracks near the surface due to the skin effect. Ultrasonic Testing (UT), usually combined with phased array systems, are capable of detecting cracks located deep in the sample, which requires both the coupling agent and the smooth surface [10–12]. EMAT is a new type of non-contact ultrasonic transducer, which has unique advantages in NDT and internal structure evaluation due to its outstanding advantages such as non-contact, no coupling agent required, flexible generation of multiple acoustic modes, and suitability for harsh environments such as high temperatures [13–15].

In electromagnetic ultrasonic inspection, different modes of ultrasonic waves are suitable for different inspection occasions, ultrasonic guided waves can be used for long-distance defect detection and structural health monitoring [16,17], while bulk waves can be used for identification, localization and imaging of local defects [18,19]. The temporal technique is a commonly used method for bulk wave in pulsed-echo mode, in which a ultrasonic wave is excited in the testing sample by an EMAT, and the internal cracks can be assessed by the ToF of the defect echo [20]. However, some internal defects with relatively small sizes compared to the ultrasonic transducer, such as cracks, are difficult to extract the defect echo because the energy of ultrasonic wave reflected back from the defect wall is too low. In order to enhance the amplitude and signal-to-noise ratio (SNR) of the EMAT signals to

 doi:10.20944/preprints202407.2152.v1

improve the detection capability of defects, many researchers have implemented parameter optimization, signal processing and new probe designs [21–24]. However, in harsh industrial environments, the above methods are not effective, because the background industrial noise may cover up the defect echoes. Therefore, using the amplitude attenuation of bottom echo to identify the tiny cracks based on inversion is more appropriate. Parra-Raad et al. designed an EMAT that could excite orthogonal shear waves and used it to identify and determine the direction of cracks through the amplitude difference [25]. But few researchers have investigated bottom crack defects with width and depth less than 1 mm by using EMAT, and our study makes up for this part and explains the rationality and advantages of using bottom echo amplitude detection in principle.

It is worth noting that in industrial inspection, the fluctuation of probe lift-off caused by vibration of the drive mechanism, non-conductive coatings, etc. can significantly affect the amplitude of EMAT signals and lead to confusion and misjudgment of defect signals [26,27]. Therefore, it is necessary to monitor the lift-off of probe in real time, and reduce the effect of lift-off on the detection signal. Xiang et al. investigated the effect of lift-off on the frequency and peak amplitude of EMAT surface wave excitation process [28]. Feng studied the effect of lift-off on Motion-Induced Eddy Current (MIEC) testing based on semi-analytical model [29]. Hu et al. proposed a method on the basis of the permanent magnetic field perturbation (PMFP) theory to compensate for the defect signal using the measured lift-off information [30]. Duan et al. designed a new type of pulsed eddy current (PEC) probe array with different lift-offs and linearly combined the signal features under different lift-offs to reduce the effect of lift-off [31], and the method was extended to EMAT [32]. The amplitude attenuation of EMAT signals due to bottom defects follows the same trend caused by the increased lift-off. Therefore, it is necessary to distinguish their differences in principle and extract a signal feature that is only affected by lift-off rather than the defect based on the multi-physical fields coupling process of EMAT, which can be used to correct the effect of lift-off on crack detection signal.

To address this research gap, we propose a novel EMAT-PEC composite sensor consisting of a butterfly coil and a pair of rectangular coils. The amplitude of EMAT signal recorded by the butterfly coil can be used to identify the tiny bottom cracks, and the PEC signals obtained by the integrated symmetrically arranged rectangular coils can be used to measure the average lift-off of the probe in real time during the scanning inspection. In order to eliminate pseudo-defect signals caused by probe jitter and to improve the accuracy of detection, we propose a multi-signal fusion method that can correct the amplitude of defect detection signal to reduce the effect of lift-off. Finally, we fabricated the composite sensor and probe for validating and applying the proposed method.

The other sections are organized as follows. Section 2 establishes a numerical theoretical model of the bulk wave EMAT and lift-off, distinguishes the effect of bottom crack and lift-off on the detection signal and designs an EMAT-PEC composite sensor. Section 3 explores the fitting relationship between multiple signals recorded by the composite sensor and lift-off using the FEM and proposes a signal fusion method for PEC and EMAT signals to correct the amplitude of defect detection signal. Section 4 focuses on the construction of an experimental platform and validation experiments to evaluate the performance of the proposed sensor and signal correction and fusion approach. Finally, Section 5 summarizes the innovations and contributions of the article and looks forward to future research directions.

2. Theory and Composite Sensor Design

2.1. Principle of bulk wave EMAT

A typical bulk wave EMAT consists of a permanent magnet, a coil and a conductor sample, as shown in Figure 1(a). Figure 1(b) shows a butterfly coil with equal spacing and same direction in the central part. Compared to the spiral coil and racetrack coil, the butterfly coil excites shear wave with a smaller divergence angle and more intensive distribution, providing stronger detectability [33].

Preprints.org (www.preprints.org) | NOT PEER-REVIEWED | Posted: 26 July 2024 doi:10.20944/preprints202407.2152.v1

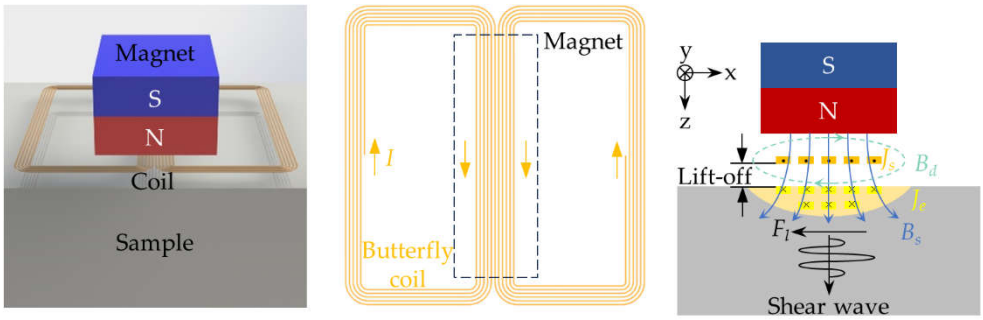

(**a**) (**b**) (**c**)

Figure 1. Schematic of the bulk wave EMAT: (**a**) Basic components of EMAT; (**b**) A butterfly coil; (**c**) The excitation process of shear wave based on the Lorentz mechanism.

The excitation process of shear wave based on the Lorentz mechanism of EMAT is illustrated in Figure 1c. A coil fed with high frequency alternating current J_s is placed near the surface of the testing sample, which generates a dynamic magnetic field B_d in the surroundings and induces an eddy current J_e in the sample. The eddy current J_e generates Lorentz force F_l in interaction with the dynamic magnetic field B_d and the biased static magnetic field B_s provided by the permanent magnet, causing high-frequency vibrations of the particles inside the sample, which excites the shear waves. Based on Maxwell's laws, the governing equations for the energy conversion process can be expressed as,

$$\nabla \times H_d = J_s , \tag{1}$$

$$B_d = \mu_0 \mu_r H_d , \tag{2}$$

$$\nabla \times E_e = - \frac{\partial B_d}{\partial t} , \tag{3}$$

$$J_e = \sigma E_e , \tag{4}$$

$$F_l = J_e \times (B_d + B_s) \approx J_e \times B_s , \tag{5}$$

where H_d denotes the dynamic magnetic field intensity, μ_0 (= $4\pi \times 10^{-7}$ H/m), μ_r denote the vacuum permeability and the relative permeability of sample, respectively. E_e denotes the electric field intensity, σ denotes the electrical conductivity of sample. In Equation (5), the dynamic magnetic field B_d can be neglected for a relatively small excitation pulse current [34].

The governing equation for the vibrations of the particles inside the sample induced by the Lorentz forces can be expressed as,

$$G \nabla^2 u + (G + \kappa) \nabla (\nabla \cdot u) + F_l = \rho \frac{\partial^2 u}{\partial t^2} , \tag{6}$$

where G, κ denote the Lamé constants of the material, u denotes the displacement of the particles inside the sample, and ρ denotes the density of the material.

The shear wave excited in pulse-echo mode propagates in the thickness direction, undergoes reflection and mode conversion at the bottom or defects, and then part of it propagates back to the surface. Based on the inverse Lorentz effect, the vibrations of the particles induced by the reflected shear wave generate an eddy current J_u under the interaction with the biased static magnetic field B_s provided by the magnet. The dynamic magnetic field generated by J_u passes the material-air boundary and is captured by EMAT. The induced eddy current J_u can be expressed as,

$$J_u = \sigma (E_u + \frac{\partial u}{\partial t}). \tag{7}$$

Preprints.org (www.preprints.org) | NOT PEER-REVIEWED | Posted: 26 July 2024 doi:10.20944/preprints202407.2152.v1

Figure 2(a) shows the reflection and mode conversion of shear wave occurring at defects of different relative sizes to the probe. Figure 2(b) illustrates their corresponding time-domain detection signals picked up by EMAT.

1. When there are no defects on the bottom, the excited shear wave is reflected at the bottom, showing several echoes in the time-domain signal. This configuration of EMAT also excites less longitudinal wave, which occurs reflection and mode conversion at the bottom to form reflected longitudinal waves, shear-longitudinal (SL) and longitudinal-shear (LS) converted waves. They are located between adjacent echoes due to their propagation speed, which are considered as noise signals, affecting defect detection. While the ToF_1 of adjacent echoes can be used to evaluate the wall thickness of the sample;
2. When there are relatively large defects to the probe on the bottom, the beam width of the shear wave excited by EMAT is smaller than the defect width, and a large portion is reflected by the defect, thus showing a changed ToF_2;
3. When there are relatively small defects to the probe on the bottom, such as cracks, the beam width is larger than the defect width, and only a small portion is reflected at the interface of the defect. The rest is reflected at the bottom or affected by the side of the defect to produce scattered waves in other directions, thus showing a changed peak value (PV) of 1st bottom echo.

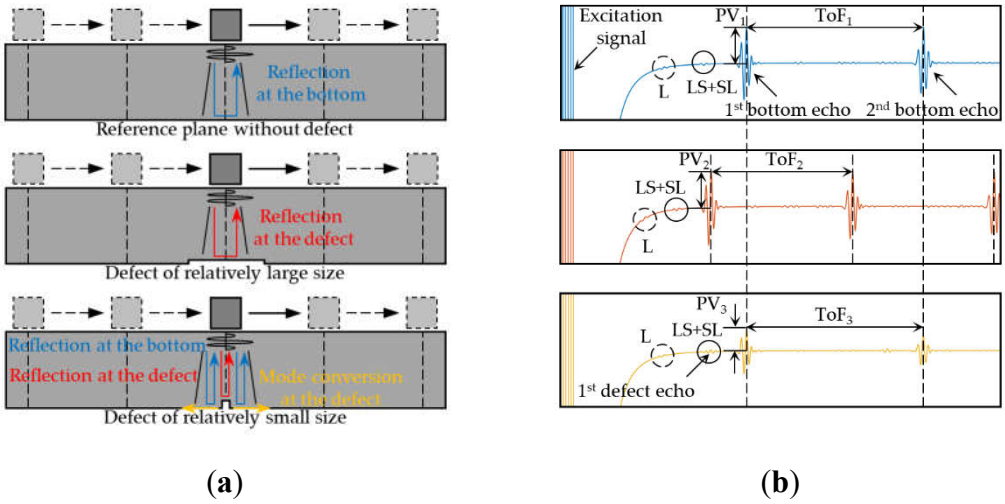

Figure 2. Pulse-echo mode for the bulk wave EMAT: (**a**) Reflection and mode conversion of ultrasonic wave at defects of different relative sizes to the probe; (**b**) Corresponding time-domain signals picked up by EMAT.

For the detection of cracks with small size, the amplitude of echo reflected by the defect is relatively small, which is not convenient to extract and is easily overlapped or confused with the converted waves described above. The amplitude of bottom echo has a relatively large SNR, the crack can be recognized and assessed by its attenuation. In combination with a scanning mechanism, the maximum attenuation of the echo amplitude can be used as the standard for the localization of crack.

The factors such as coil design parameters and lift-off of probe also affect the signal of EMAT, resulting in variations in its amplitude, so it is necessary to study the mechanism of their influence.

2.2. Effect of Lift-Off on Lorentz Force of Bulk Wave EMAT

As shown in Figure 3, to simplify the analysis, the central working region of the butterfly coil is approximated as a thin current sheet of width w and the whole space is regarded as the existence of a constant and uniformly distributed magnetic field $B_{d,z}$. The boundary between the sample and the air is set to be the x-axis, and the left edge of the current sheet is set to be the z-axis. z>0 space is filled with the sample made of conductive material, and $z<0$ space is filled with air. We assume that the turns per unit length of the coil is n and the current flowing through the coil is I. In this two-dimensional approximate model, Equation (1)-(3) can be simplified as,

 doi:10.20944/preprints202407.2152.v1

$$\frac{\partial H_x^S}{\partial z} - \frac{\partial H_z^S}{\partial x} = J_{e,y}, \tag{8}$$

$$\frac{\partial E_y}{\partial z} = \mu_0 \mu_r \frac{\partial H_x}{\partial t}, \tag{9}$$

$$\frac{\partial E_y}{\partial x} = -\mu_0 \mu_r \frac{\partial H_z}{\partial t}. \tag{10}$$

Combining Equations (4), (9), (10), we get,

$$\left(\frac{\partial^2}{\partial x^2} + \frac{\partial^2}{\partial z^2}\right) H_x - jw\sigma\mu_0\mu_r H_x = 0. \tag{11}$$

In air, the H_x^A satisfies,

$$\left(\frac{\partial^2}{\partial x^2} + \frac{\partial^2}{\partial z^2}\right) H_x^A = 0. \tag{12}$$

The tangential magnetic field at the origin (0,0) provided by the current element $nIdx$ at (x,z) can be expressed as,

$$dH_x^A = \frac{nIdx}{2\pi(x^2+z^2)} \cdot \frac{2z}{\mu_r + 1}. \tag{13}$$

We assume that the charge is uniformly distributed on the current sheet $(X,-l)$, $X \in (0, w)$, and l denotes the lift-off of the coil. At the boundary between the sample and the air, the tangential magnetic field satisfies the boundary conditions, thus the tangential magnetic field at $(x,0)$ provided by the entire current sheet can be expressed in the integral form of Equation (13) as,

$$H_x^S(x,0) = H_x^A(x,0) = \frac{nI}{\pi(\mu_r+1)} \cdot \int_0^w \frac{[0-(-l)]dX}{(x-X)^2 + [0-(-l)]^2} = \frac{nI}{\pi(\mu_r+1)} \cdot \left[\arctan\left(\frac{x}{l}\right) - \arctan\left(\frac{x-w}{l}\right)\right]. \tag{14}$$

In sample, the H_x satisfies,

$$\frac{\partial^2 H_x^S(x,z)}{\partial z^2} - q^2 H_x^S(x,z) = 0, \tag{15}$$

where $q = -(1+j)/\delta$, δ denotes the skin depth of the sample,

$$\delta = \sqrt{\frac{2}{w\mu_r\mu_0\sigma}}. \tag{16}$$

Combining Equations (14), (15), we obtain,

$$H_x^S(x,z) = \frac{nI}{\pi(\mu_r+1)} \cdot e^{-(j+1)\frac{z}{\delta}} \cdot \left[\arctan\left(\frac{x}{l}\right) - \arctan\left(\frac{x-w}{l}\right)\right]. \tag{17}$$

Substituting Equation (17) into Equation (8), we get,

$$J_{e,y}(x,z) = \frac{\partial H_x^S(x,z)}{\partial z} = \frac{(1+j)}{\delta} H_x^S(x,z). \tag{18}$$

The eddy current density inside the sample at x can be expressed as,

$$J_{e,y}(x) = \int_0^\infty J_{e,y}(x,z)dz \propto \left[\arctan\left(\frac{x}{l}\right) - \arctan\left(\frac{x-w}{l}\right)\right]. \tag{19}$$

Preprints.org (www.preprints.org) | NOT PEER-REVIEWED | Posted: 26 July 2024 doi:10.20944/preprints202407.2152.v1

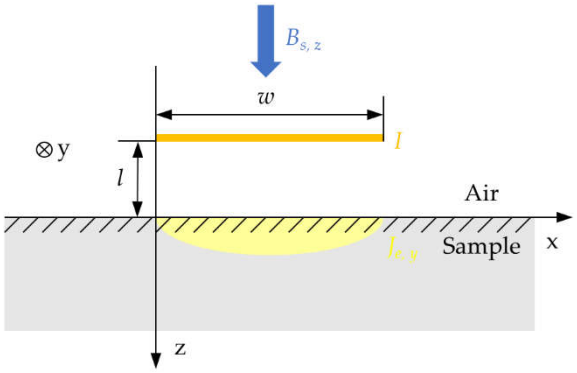

Figure 3. Two-dimensional simplified model of butterfly coil EMAT.

The Equation (19) shows that the distribution of J_e is mainly determined by the width w and lift-off l together, provided that other parameters are constant. Setting w = 2mm, the profiles of normalized J_e with different lift-offs are shown in Figure 4(a). In the case of constant w, J_e is symmetrically distributed about $x = w/2$, with the peak value occurring at that point, i.e., the center of the coil. And as l increases, J_e decreases but the overall profile becomes wider. Assuming that the static magnetic field is constant and uniform, F_l can be regarded as positively correlated with the magnitude of J_e and be considered to have the same spatial distribution with J_e. Therefore, at a certain excitation frequency, the energy and radiation range of the shear wave excited by EMAT are mainly affected by the coil design parameter w and the lift-off distance l.

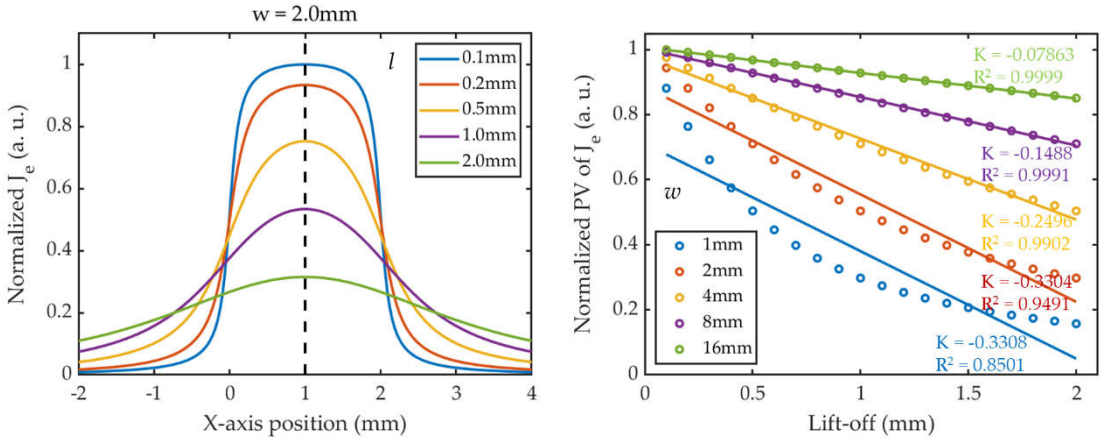

(**a**) (**b**)

Figure 4. The results of numerical calculations from Equation (19): (**a**) The profiles of normalized J_e under different l; (**b**) The curves of normalized PV of J_e vs. lift-offs under different w.

When $x = w/2$, Equation (19) can be expressed as,

$$J_{e,y}(\frac{w}{2}) \propto 2\,arctan\,(\frac{w}{2l}). \tag{20}$$

Equation (20) and Figure 4(b) show that the relationship between PV of J_e and l is consistent with an inverse tangent function. And in the same lift-off fluctuation range, as w increases, the absolute value of the slope for the curves also decreases, showing that coils with larger w have better resistance to lift-off interference. However, the coil with the larger width excites a wider beam of shear wave, resulting in lower sensitivity to cracks with small sizes, and therefore a compromise is needed for the parametric design of w.

The coil is affected by the change of the magnetic field in surroundings and generates a corresponding voltage signal. The eddy current J_e and the input excitation current J_s contribute to the variation of the PEC signal, while the eddy current J_u induced by the ultrasonic echo contributes to

 doi:10.20944/preprints202407.2152.v1

the variation of EMAT signal. The lift-off fluctuation mainly affects the intensity of J_e, which leads to an indirect effect on J_u, causing changes in both EMAT and PEC signals, while the defect directly affects the intensity of J_u, causing changes in the EMAT signal without affecting the PEC signal.

However, in industrial inspections, lift-off fluctuation is a non-negligible problem, and the EMAT signal is highly susceptible to lift-off, so it is necessary to design a sensor that can resist lift-off interference and to propose a method for real-time amplitude correction of EMAT signal during scanning detection.

2.3. EMAT-PEC Composite Sensor Design

When the outer surface of sample is not smooth, there perhaps exists the rough wax, attached dirt, coating loss, or coating deformation [26], as shown in Figure 5. The probe will be subjected to a reaction force perpendicular to the tangential direction of the outer surface, which can cause the probe vibration. Moreover, the probe usually is combined with the mechanical mechanism in scanning inspection, and the random vibration of the machinery will also cause fluctuation of lift-off. All of the above will affect the accuracy and consistency of the inspection results.

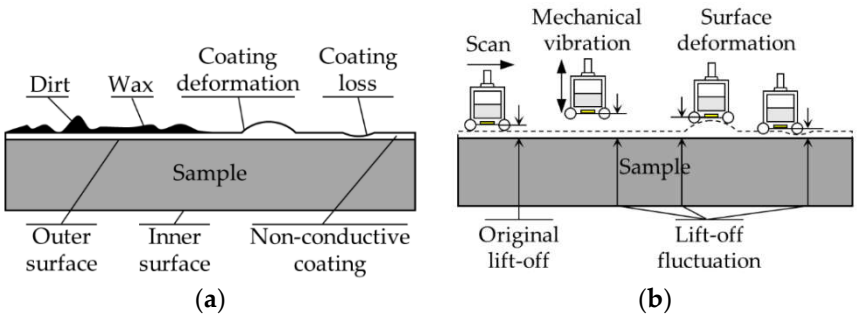

Figure 5. Schematic of the lift-off fluctuation in the scanning detection process: (**a**) Uneven outer surface of sample; (**b**) The Lift-off fluctuations in several scenarios.

Combining the analysis in Subsection 2.1 and 2.2, it can be concluded that the mechanisms of bottom crack and lift-off fluctuation resulting the variation of EMAT signals are different. The former leads to the reflection, the scattering and mode conversion of the ultrasonic wave at the defect, resulting in the energy reduction of the ultrasonic echo. While the latter affects the intensity of the induced eddy current during excitation, weakening the energy of the excited ultrasonic wave.

In this paper, a compact EMAT-PEC composite sensor is designed with the structure shown in Figure 6. The composite sensor is center-symmetrical with a butterfly coil and two rectangular coils, which are located in the same plane. During each detection cycle, a pulse excitation is passed into the butterfly coil, and each rectangular coil senses the change of magnetic field in surroundings to generate PEC signals. When the probe is operating smoothly, the waveform of the PEC signal is basically unchanged, which can be regarded as the density of induced pulsed eddy current distributed on the surface of the sample is the same in each cycle, so it can be inferred that there is no change in the lift-off of the probe, and the variation of amplitude of EMAT signal can be used as a judgement for detecting the defect. When the probe undergoes lift-off fluctuation, the primary magnetic field generated by the excitation current does not cause the change of PEC signals, because of the constant relative position between the EMAT coil and the PEC coils. But the lift-off fluctuation will affect the pulsed eddy current density and the secondary magnetic field generated by it, resulting in the change of PEC signals. Therefore, extracting the PV of the PEC signals can characterize the lift-off information at the points of the symmetric rectangular coils and measure the average lift-off, which can be used to evaluate the variation in lift-off of the whole probe.

Preprints.org (www.preprints.org) | NOT PEER-REVIEWED | Posted: 26 July 2024 doi:10.20944/preprints202407.2152.v1

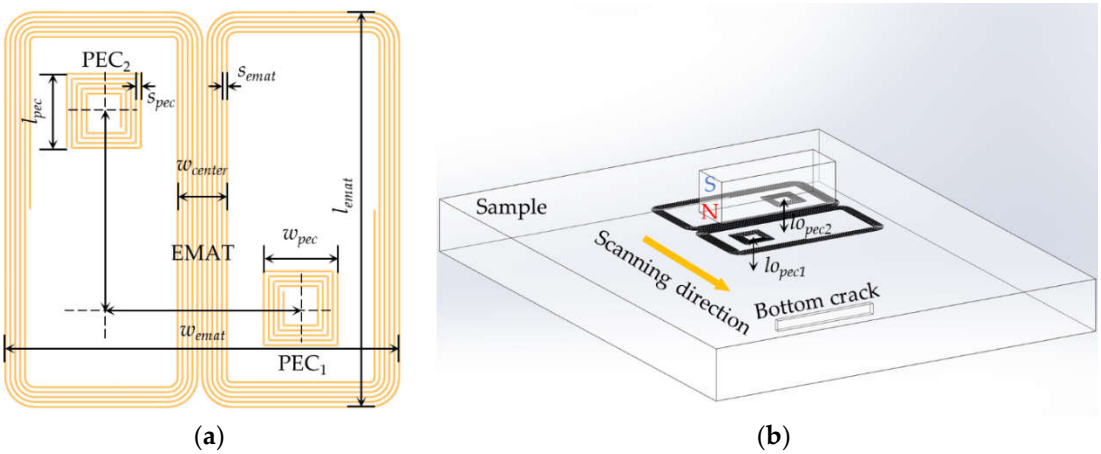

(**a**) (**b**)

Figure 6. Schematic diagram of EMAT-PEC composite sensor: (**a**) Components of composite sensor; (**b**) Side view of the whole probe.

The proposed composite sensor has the following characteristics:

1. The butterfly coil can produce unidirectional and uniform shear wave with a small divergence angle, which has a good detection ability for tiny cracks perpendicular to the polarization direction;
2. The symmetric rectangular coils are used to measure the average lift-off of the probe, which can effectively improve the accuracy of the measurement in special industrial scenarios such as probe tilting, and achieve better applicability.
3. In each cycle, the PEC and EMAT signals originate from the same excitation signal, so it is easier to synchronize the acquisition of the PEC and EMAT signals and match them compared to the addition of other displacement sensors, which has positive implications for subsequent signal fusion and correction.
4. The proposed composite sensor uses only a single excitation signal to avoid crosstalk between multiple signals and improve energy utilization of EMAT. The use of one transmitter and multiple receivers reduces the complexity of the circuit system, and the PEC signals can be extracted through a low-pass filter in the appropriate frequency band.

Based on the analysis in Subsection 2.2 and Figure 4(b), we determined the w_{center} to be 4 mm for the consideration of balancing the ability of tiny cracks detection and the resistance to lift-off fluctuation. The geometrical parameters of the composite sensor were optimized in our previous work [32], as shown in Table 1.

Table 1. Parameters of the EMAT-PEC symmetric composite sensor.

Object	Parameter	Symbol	Value
EMAT	width	w_{emat}	16mm
	length	l_{emat}	16mm
	lift-off	lo_{emat}	0.1mm
	wire diameter	d_{emat}	8mil
	wire spacing	s_{emat}	16mil
	wire height	h_{emat}	0.035mm
	turns	n_{emat}	11
PEC_1, PEC_2	width	w_{pec}	4mm
	length	l_{pec}	4mm
	lift-off	lo_{pec}	0.1mm
	wire diameter	d_{pec}	8mil

 doi:10.20944/preprints202407.2152.v1

	wire spacing	d_{pec}	16mil
	wire height	h_{pec}	0.035mm
	turns	n_{pec}	5

3. Simulation Analysis and Method

3.1. Finite Element Modeling

In order to further explore the ability of the proposed composite sensor to detect small-sized bottom cracks under the influence of lift-off fluctuation, a 2D FEM was established using COMSOL Multiphysics 6.2. The FEM was divided into six regions: permanent magnet, EMAT coil, PEC coils, sample, air, and infinite element domain, as shown in Figure 7(a), and the additional parameters of the 2D FEM are shown in Table 2. The material of the permanent magnet was set as N52 NdFeB in the COMSOL material library, and the remanent flux density was set to 1.21T. The material of the coil was set to copper, with a density of 8960 kg/m3 and a conductivity of 5.998×10^7S/m. The excitation current injected into the coil consisted of a 3-cycle tone-burst signal with a center frequency of 5 MHz modulated by the Hanning window, as indicated in Figure 7(c). The material of the sample was set to be steel with a density of 7850 kg/m3, Young's modulus of 200×10^9 Pa and Poisson's ratio of 0.3. The electrical conductivity of the sample was 4.032×10^6S/m, and the permeability followed the B-H curve, as indicated in Figure 7(d). The original lift-off of the coil was set to 0.1mm and the original lift-off of the magnet was set to 0.5mm. The infinite element domain was set up around the air to ensure the accuracy of the magnetic field of the permanent magnet at different lift-offs. After building the mesh, the minimum element quality was 0.4558 and the average element quality was 0.9513.

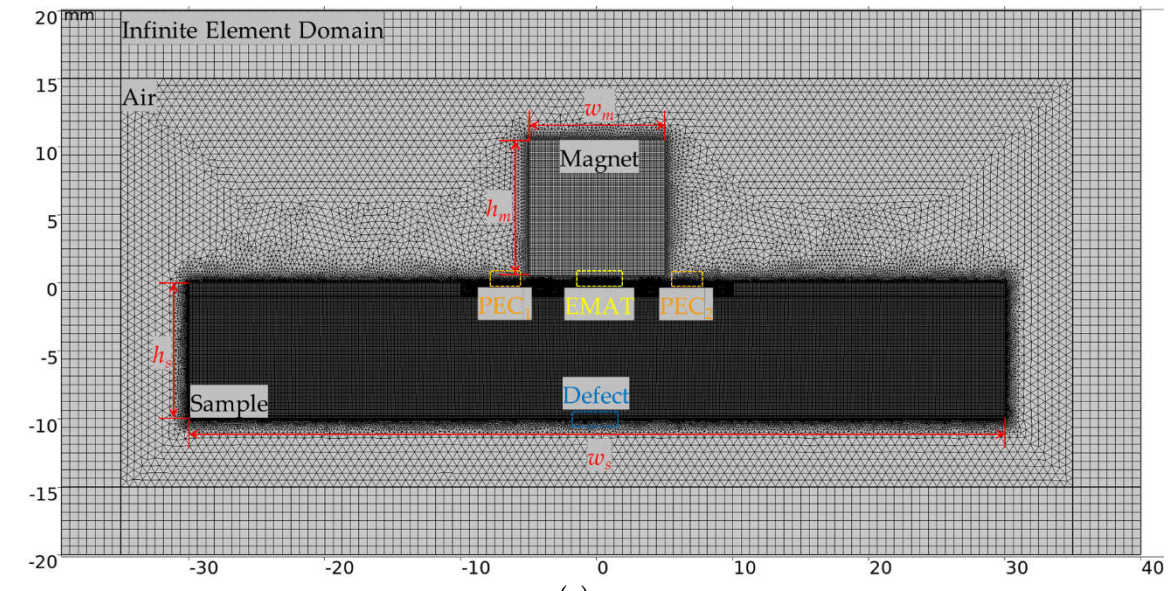

(**a**)

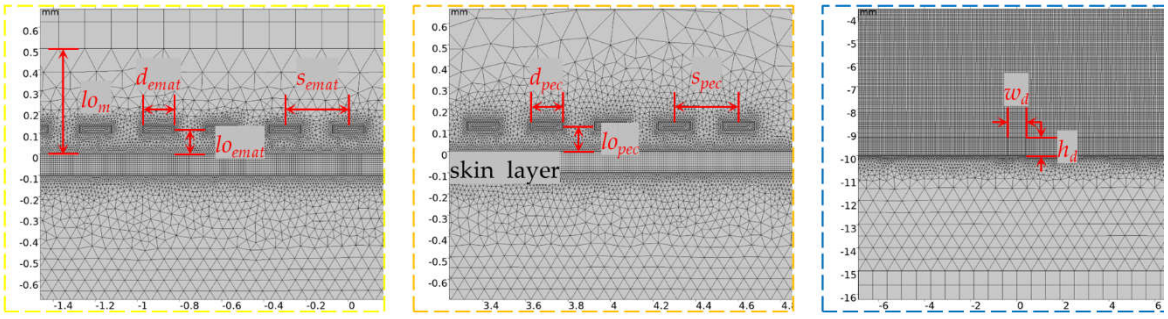

(**b**)

Preprints.org (www.preprints.org) | NOT PEER-REVIEWED | Posted: 26 July 2024 doi:10.20944/preprints202407.2152.v1

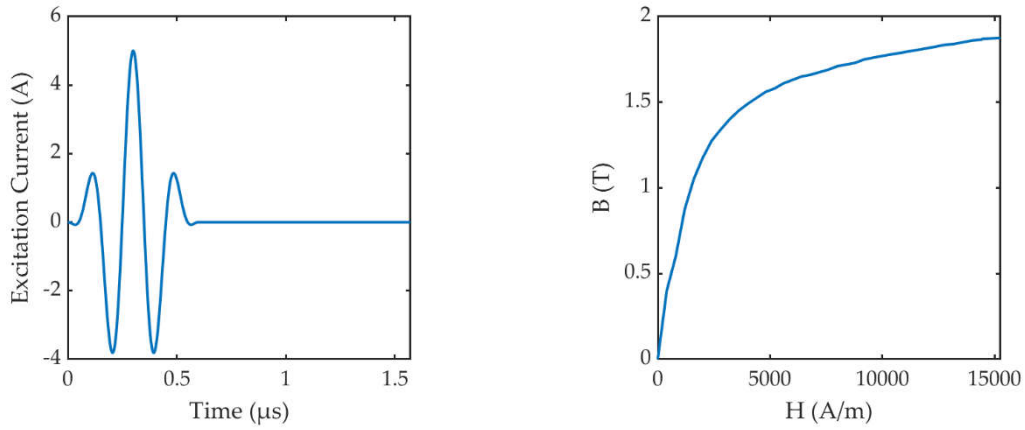

(**c**) (**d**)

Figure 7. Schematic diagram of 2D FEM in COMSOL: (**a**) Overall view with mesh division; (**b**) Partial enlarged views of the components; (**c**) Excitation current of the EMAT; (**d**) B-H curve of the sample.

Table 2. Additional parameters of 2D FEM.

Object	Parameter	Symbol	Value
magnet	width	w_m	10mm
	height	h_m	10mm
	lift-off	lo_m	0.5mm
	remanent flux density	B_s	1.21T
sample	width	w_s	60mm
	thickness	h_s	10mm
	density	ρ	7850kg/m^3
	permeability	μ	B-H curve
	electrical conductivity	σ	4.032×10^{6}S/m
	Young's modulus	E	200×10^{9}Pa
	Passion's ratio	ε	0.33
excitation current	center frequency	f_c	5MHz
	cycle	n	3

To simulate the performance of the EMAT in pulse-echo mode for measuring bottom defect, the Transient Solver in COMSOL was employed to calculate the distributions of electromagnetic and acoustic fields for the time period of 0 to 2.4×10^{-5}s ($1/f_c$*120) in steps of 1×10^{-7}s ($1/f_c$/20). Meanwhile, we added Coil Geometry Analysis in FEM to directly obtain the EMAT and PEC signals picked up by the coils.

3.2. Crack Detection with Different Sizes

In order to study the effect of cracks with different depths and widths on the amplitude of bottom echo recorded by EMAT, the rectangular area at the middle of the bottom of the steel sample was replaced as air to simulate the bottom crack, as shown in Figure 7(b). And then, four groups of simulation models with various crack depths (0.2, 0.4, 0.6 and 0.8mm) as well as for different crack widths (0.2, 0.4, 0.6 and 0.8mm) were set up. Figure 8 shows the 1st bottom echo signals of EMAT, and the signal of 'Crack width = 0.0mm' indicates the reference signal without defect. The simulation results show that the presence of defect causes the attenuation of the bottom echo. And as the defect width and depth increases, the amplitude of the bottom echo decreases.

 doi:10.20944/preprints202407.2152.v1

In Figure 8a–c, we can observe that the crack echo partially overlaps with the side flaps of the bottom echo, causing the signal features of crack echo to be difficult to extract when the depth of the crack is relatively smaller than the wavelength ($\lambda \approx 0.64$mm). In Figure 8(d), as the crack width increases, the amplitude of the crack echo increases. But even when the bottom echo amplitude decays to less than half of the reference signal amplitude, the crack echo amplitude fails to equal the bottom echo amplitude. Therefore, it is crucial to analyze the causes and understand the interaction of the shear wave with the crack at bottom.

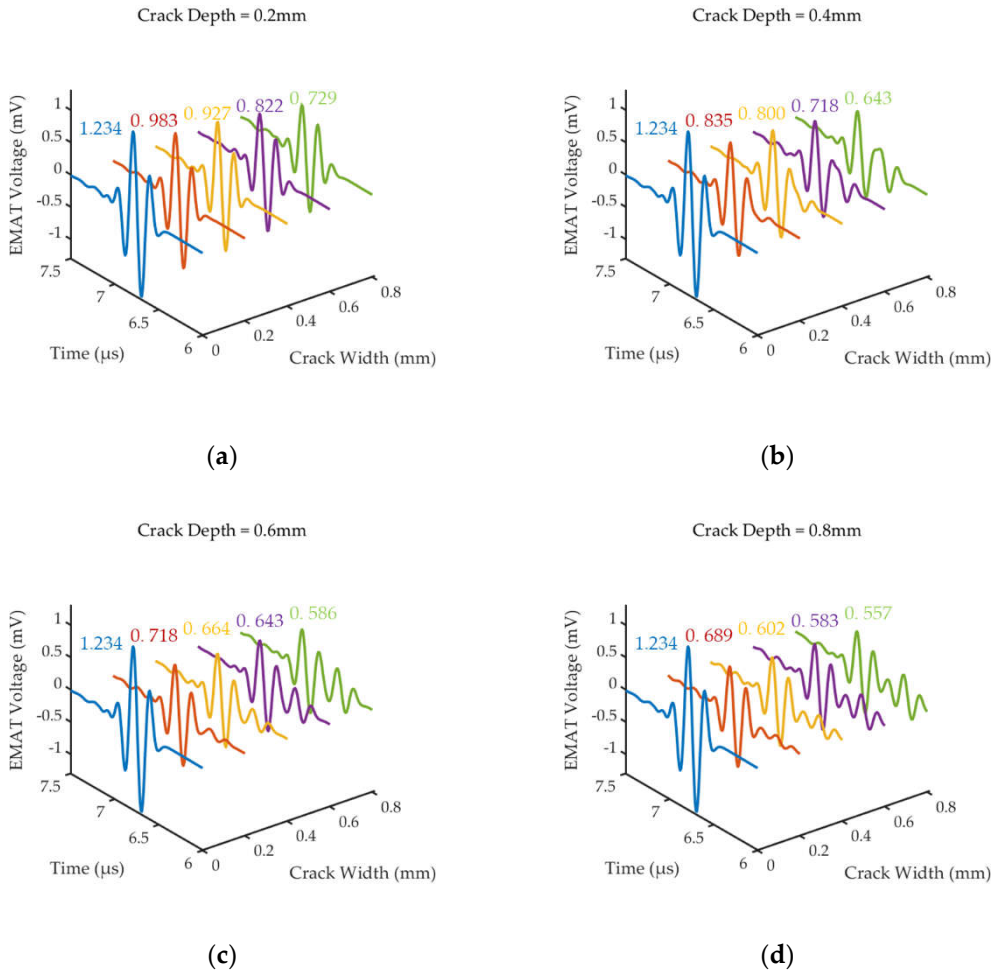

Figure 8. EMAT signals under cracks of different widths w_d and depths h_d: (**a**) Crack depth = 0.2mm; (**b**) Crack depth = 0.4mm; (**c**) Crack depth = 0.6mm; (**d**) Crack depth = 0.8mm.

Figure 9 illustrates the distributions of Von Mises Stress inside the sample at two different moments for the detection of a crack with 0.8mm depth and 0.2mm width. Figure 9(a) shows that only a small portion of the incident shear wave polarized perpendicular to the crack is reflected at the interface of the crack, while the rest continues to propagate downward and interacts with both sides of the crack. Figure 9(b) shows that the shear wave scatters at the tips of the crack and undergoes a mode conversion with the interaction of the sides of the crack, generating Rayleigh waves [35]. Rayleigh waves propagate along the bottom of the sample to the sides, and will not be recorded by EMAT, resulting in further attenuation of the amplitude of the bottom echo signal. Moreover, it can be found that Rayleigh waves have a larger amplitude relative to the reflected wave of crack in Figure 9(b), which explains why the attenuation of the bottom echo signal is larger than the amplitude of the crack echo signal.

 doi:10.20944/preprints202407.2152.v1

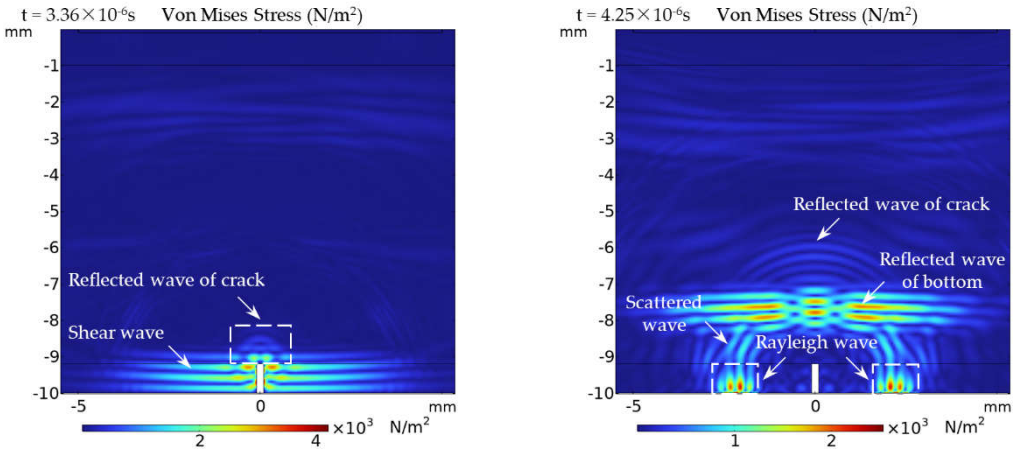

(**a**) (**b**)

Figure 9. The simulation results of the acoustic field for the interaction of shear wave with the defect at bottom: (**a**) T=3.36×10⁻⁶s; (**b**) T=4.25×10⁻⁶s.

Based on the above analysis, we can conclude that in the detection of cracks with small size, using the amplitude of the bottom echo as a signal feature to implement the detection has the following advantages:

1. The feature of the 1st bottom echo amplitude is easily extracted and the ToF between adjacent echoes can be used to synchronize the thickness measurement of the sample;
2. The amplitude of bottom echo is much larger than the amplitude of small-size crack echo, and a better SNR can be achieved;
3. Due to the complex reflection, scattering and mode conversion at crack-like defects, the crack echo is difficult to be completely recorded by EMAT. Based on the inversion perspective, the amplitude attenuation of the bottom echo reflects the interaction of shear wave with the crack at bottom. The rate of change on bottom echo amplitude due to the crack is larger than on defect echo amplitude, and a higher detection sensitivity can be achieved.

3.3. Effect of Lift-Off on EMAT and PEC Signals

In Subsection 2.2, we consider the static magnetic field provided by the permanent magnet as a constant and uniformly distributed in order to simplify the analysis. However, in the actual probe fabrication, the relative position between the permanent magnet and the coil is fixed, and when the lift-off of the coil is changed, the permanent magnet will change accordingly. In order to analyze the effect of lift-off on the EMAT and PEC signals, and obtain the accurate fitting relationships, which can be used to reduce the interference of probe jitter and lift-off fluctuation, we set up a group of simulation models with different lift-offs ($lo_{emat} = lo_{pec}$ = {0.1, 0.2, 0.3, 0.4, 0.5, 1.0, 1.5, 2.0mm}), as shown in Figure 7b, and the lift-off of magnet lo_m is equal to lo_{emat} plus 0.4mm.

The skin depth of the steel sample calculated by Equation (16) is about 5.5×10⁻⁶m, and thus 2D cut line between point (-5mm, -0.005mm) to point (5mm, -0.005mm) is plotted in the datasets of the simulation results in order to analyze the distributions of B_y, J_e, and Von Mises stress in the energy conversion region of EMAT.

Figure 10(a) shows the simulation results of J_e, which are in general agreement with the theoretical calculations in Subsection 2.2. Figure 10 (b) and 10 (c) show the distribution of magnetic field in the y-direction and Von Mises Stress, respectively, and their amplitudes decrease with increasing lift-offs, which demonstrates that the lift-off fluctuation of the magnet further affects the accuracy of the detection results. Figure 10(d) illustrates that the fitting curve of J_e from the FEM is shifted upwards from the theoretical calculation as the lift-off increases. The phenomenon can be explained by Equation (17), the FEM added to simulate the lift-off variation of the magnet, and based on the B-H curve of the ferromagnetic material, the relative permeability μ_r decreases with the reduction of the applied magnetic field, thus the simulated J_e is slightly larger than the calculated

Preprints.org (www.preprints.org) | NOT PEER-REVIEWED | Posted: 26 July 2024 doi:10.20944/preprints202407.2152.v1

value. Moreover, compared to the magnet, the lift-off fluctuation of the coil has a greater effect on the intensity of ultrasonic wave, which is severely decayed under the combination of these two effects.

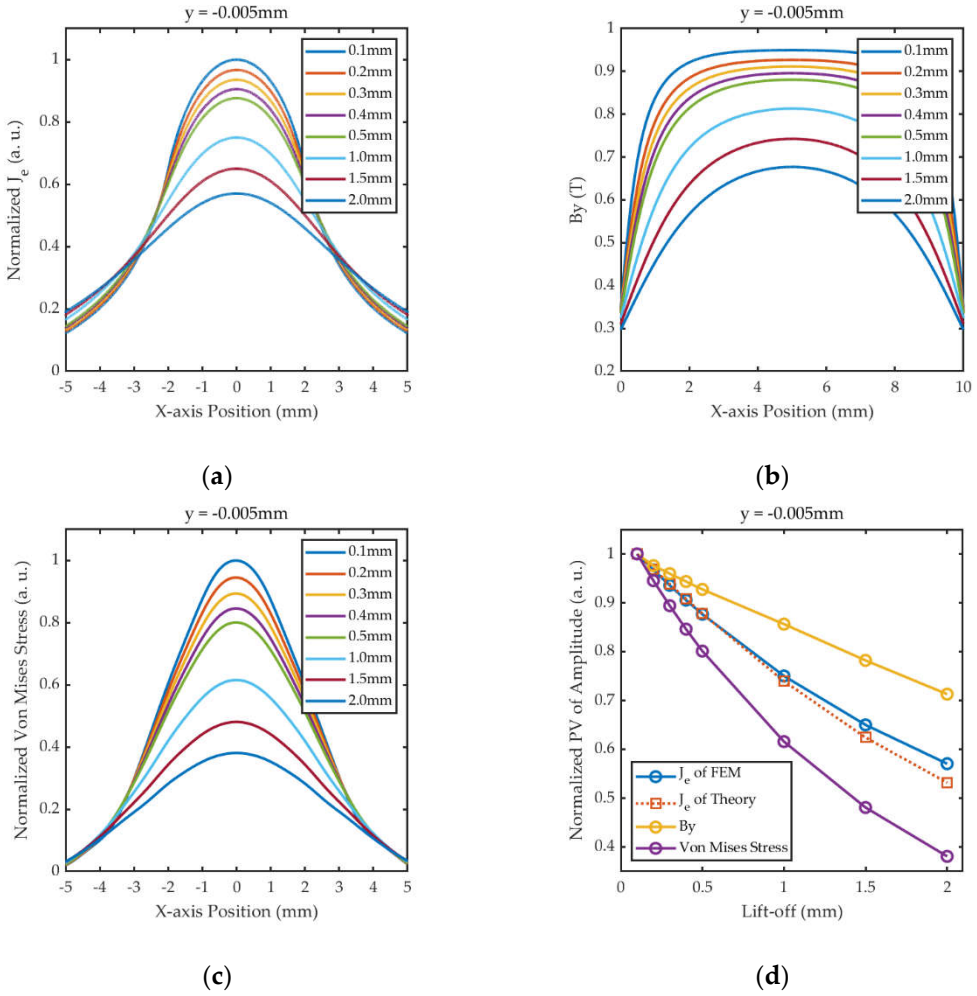

Figure 10. Simulation results of physical field distributions at 2D cut line between point (-5mm, -0.005mm) to point (5mm, -0.005mm) at 3×10^{-7}s under different lift-offs: (**a**) Distribution of J_e; (**b**) Distribution of B_y; (**c**) Distribution of Von Mises Stress; (**d**) Fitting curves of normalized PV of amplitude.

Based on Coil Geometry Analysis in COMSOL, we directly extracted the voltage signals of the EMAT coil and PEC coils under different lift-offs, as shown in Figure 11(a) and 11(b), respectively. The voltage signals picked up by PEC_1 and PEC_2 coils are identical when the plane of composite sensor is horizontal. Figure 11(c) and 11(d) correspondingly illustrate the fitting curves of PV_{EMAT} and PV_{PEC} to lift-offs. With the designed coil parameters and configurations, the fitting curve of the PV_{PEC} is highly linear with the R-square of 0.9934. This is consistent with the theoretical prediction in Subsection 2.2 and PV_{PEC} can be used as an appropriate feature to measure the lift-off of the probe. The relationship between PV_{PEC} and lift-offs can be expressed as,

$$PV_{PEC1} = k_1 \times lo_1 + b_1,\ PV_{PEC2} = k_2 \times lo_2 + b_2. \tag{21}$$

While the linearity of the fitting curve of PV_{EMAT} is poor with the R-square of only 0.9584. After taking logarithm of PV_{EMAT}, the linearity of the fitting curve of $\ln(PV_{EMAT})$ and lift-offs is better with the R-square up to 0.9999, which is consistent with the study of [36]. The relationship between PV_{EMAT} and lift-offs can be expressed as:

$$PV_{EMAT} = b_3 \times e^{-k_3 \times lo_3}. \tag{22}$$

Preprints.org (www.preprints.org) | NOT PEER-REVIEWED | Posted: 26 July 2024 doi:10.20944/preprints202407.2152.v1

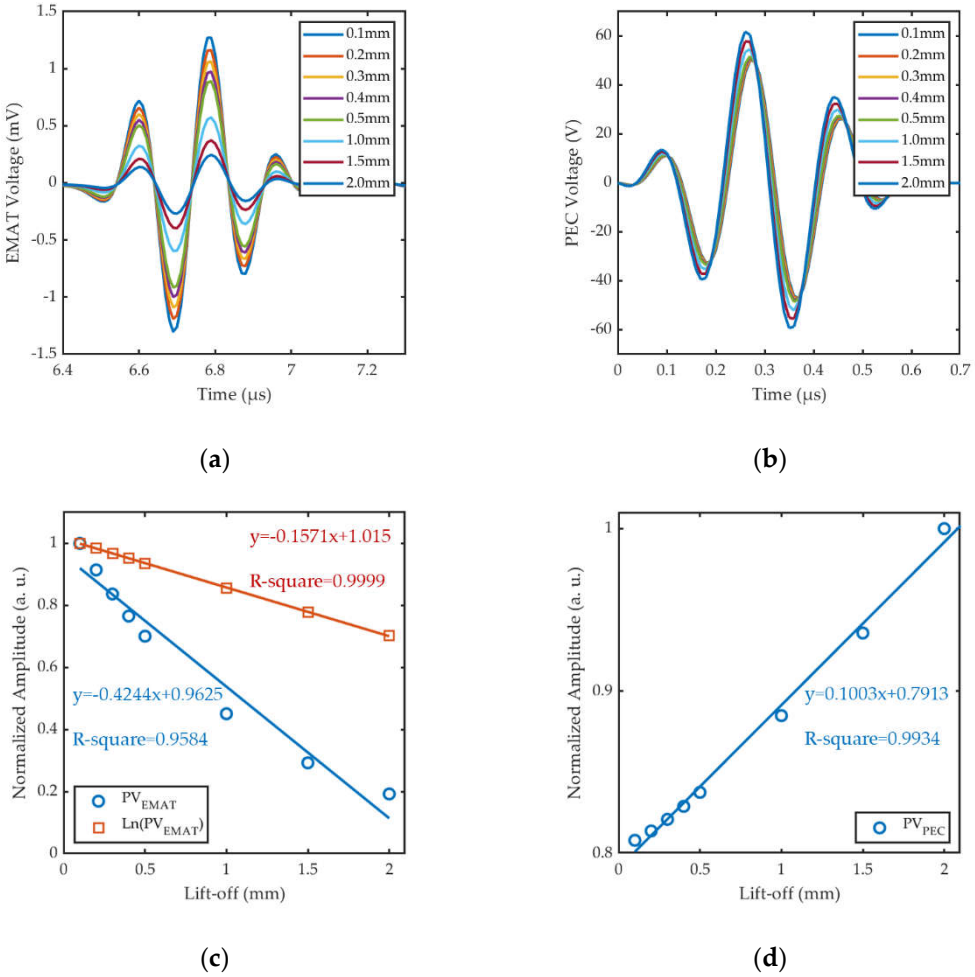

Figure 11. Simulation results of coil voltage under different lift-offs: (**a**) EMAT signals; (**b**) PEC signals; (**c**) Comparison of the fitting curves of PV_{EMAT} and $ln(PV_{EMAT})$; (**d**) Fitting curve of PV_{PEC}.

3.4. Real-Time Signal Correction and Fusion Method

In Subsection 3.3, we observe the fitting relationships between the two detection signals and the lift-offs extracted by the composite sensors. Subsequently, we propose a real-time detection signal correction and fusion method. The flowchart of signal correction and fusion is shown in Figure 12. The specific steps are as follows:

1. Step 1 is calibration. At the reference plane of the tested sample, a set of EMAT signals and PEC signals under the known lift-offs are extracted using the composite sensor to plot the fitting curves between each signal and lift-offs and determine the fitting parameters.
2. Step 2 is the measurement of lift-off. During the crack detection, the peak value of PEC signals PV_{PEC1} and PV_{PEC2} picked up by PEC_1 and PEC_2 coils are substituted into the calibrated fitting curves to calculate the average lift-off of the composite sensor in real time.
3. Step 3 is the correction of detection signals. Based on the fitting curve between EMAT signal and lift-offs, the formula for the signal correction factor can be get, and then the measured lift-off is substituted into the formula to calculate the value of correction factor, and finally the correction factor is multiplied by PV_{EMAT} to obtain the crack detection signal without interference of lift-off.
4. Step 4 is the fusion of detection signals. Combining the measurement and correction processes of steps 2 and 3, we can fuse the PV_{PEC1}, PV_{PEC1} and PV_{EMAT} signals to form a new fusion signal which is unaffected by lift-offs.

 doi:10.20944/preprints202407.2152.v1

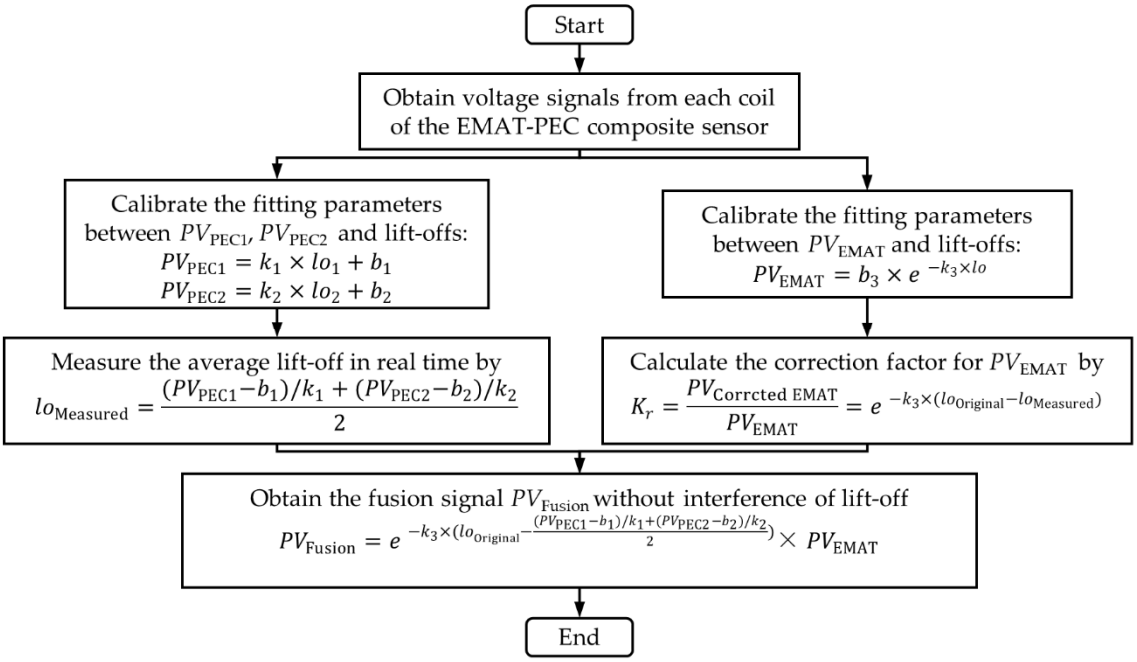

Figure 12. The flowchart of the signal correction and fusion under lift-off fluctuation.

The proposed composite detection method utilizes the lift-off measured from the PEC method to correct the detection signal of EMAT, compensating for the effect of lift-off fluctuation in the process of crack detection, which allows for a consistent assessment of the defect size inversion under different lift-offs. It should be noted that, in practice, it may happen that the lift-off is not uniform on both sides of the sensor, and therefore the average lift-off measured at two points by the centrally symmetric PEC coils is used as the equivalent lift-off for EMAT coil.

4. Experiment

4.1. Experimental Setup

In order to validate the detection performance of the proposed composite sensor, the composite sensor was fabricated and the experimental system of EMAT-PEC composite detection was established, as shown in Figure 13. The EMAT-PEC composite sensor was excited by a PR5000 EMAT Pulser-Receiver (sonemaT, UK), and the details of instrument parameters and performance are described in [15]. And two oscilloscopes were used to display the waveforms of the EMAT and PEC signals, respectively. The composite detection coils were fixed in an epoxy wear-resistant layer with a thickness of 0.2 mm, i.e., the original lift-off of the probe was determined to be 0.2 mm. The original lift-off of the permanent magnet was 1.0 mm, and the area between the detection coil and the magnet was filled with a copper foil to avoid interference caused by the eddy current generated inside the permanent magnet. A pair of rollers were set on both sides of the probe to minimize friction during scanning detection. The probe was fixed on a three-axis motion platform, which could drive the probe along the x-axis and y-axis for scanning detection and along the z-axis to simulate lift-off fluctuation. PC was used to control the three-axis motion platform while analyzing and processing the detection signals. The other parameters of the composite sensor are consistent with the parameters of FEM in Section 3.

Preprints.org (www.preprints.org) | NOT PEER-REVIEWED | Posted: 26 July 2024 doi:10.20944/preprints202407.2152.v1

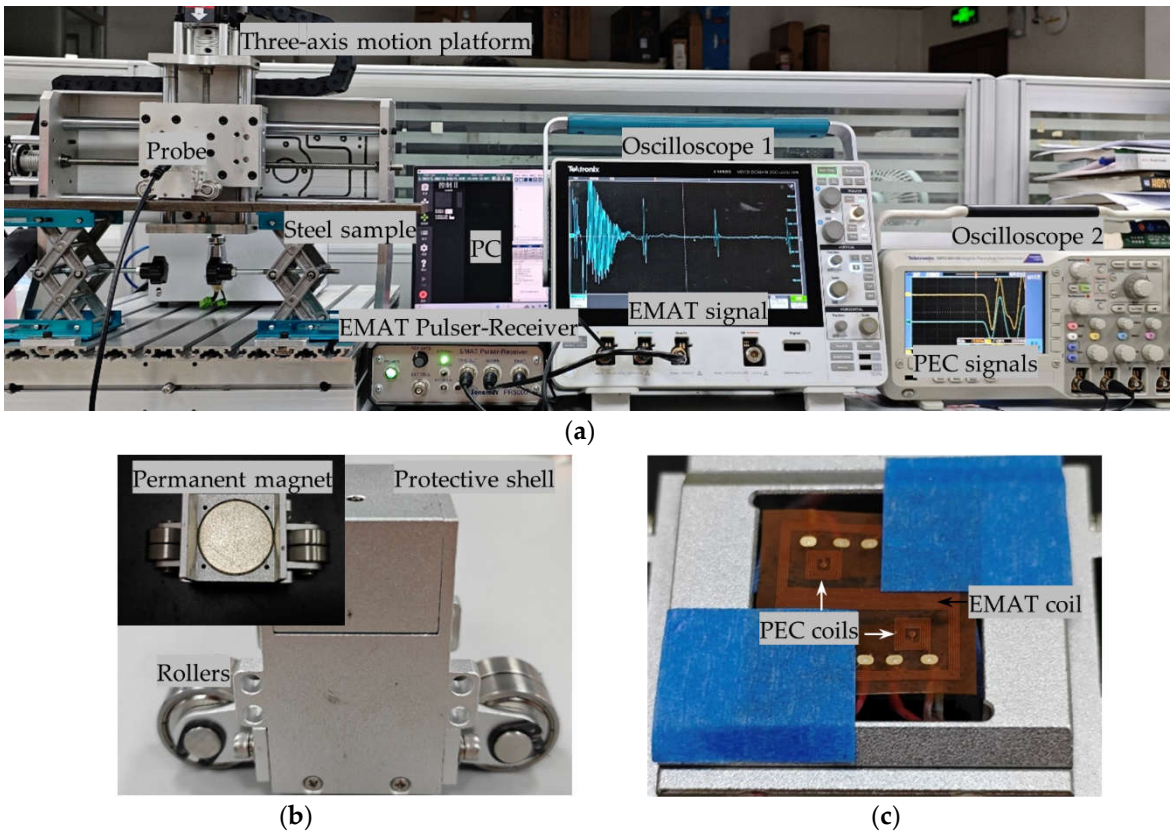

Figure 13. Experimental system of EMAT-PEC composite detection: (**a**) Experimental platform setup; (**b**) Probe structure; (**c**) Proposed EMAT-PEC symmetric composite sensor.

One side of the steel plate was manually machined with the cracks of different sizes, as shown in Figure 14. During the experiment, the probe was placed on the front side of the steel plate, and the cracks were distributed on the back side of the steel plate.

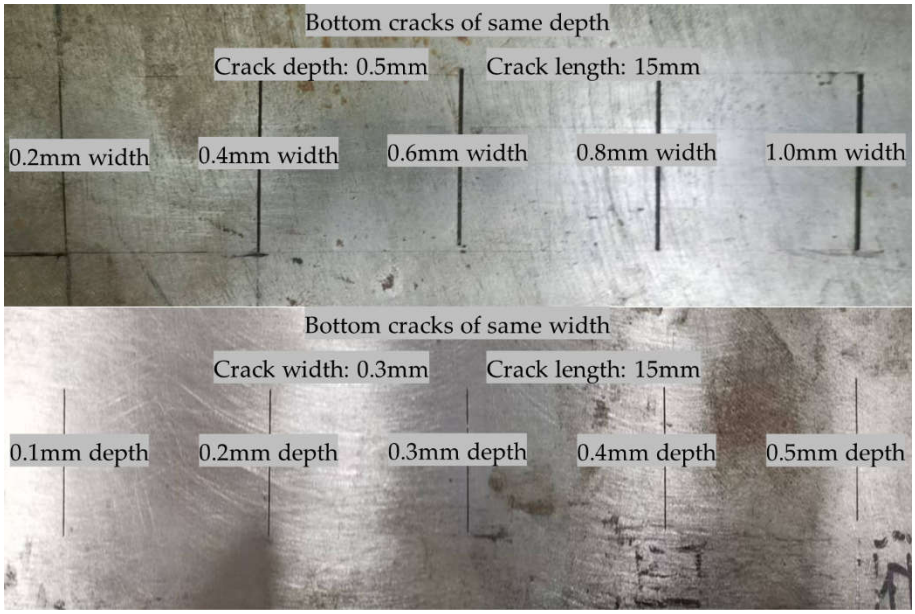

Figure 14. Size of manually machined different cracks on the bottom of steel sample.

 doi:10.20944/preprints202407.2152.v1

4.2. Results and Discussion

4.2.1. Detection of Bottom Cracks at Different Widths

Figure 15 shows the specific waveforms and *PV*EMAT under the cracks of different widths. The thickness of testing steel sample is 10mm. The experimental results show that the signal amplitude decreases with the increase of defect width, which is consistent with the law of the simulation results in Subsection 3.2. For the crack as small as 0.2 mm in width, the sensor still has good detection capability. The defect echo can be observed in Figure15(a), but its amplitude and rate of change are smaller than the bottom echo, which confirms the analysis in Subsection 3.2.

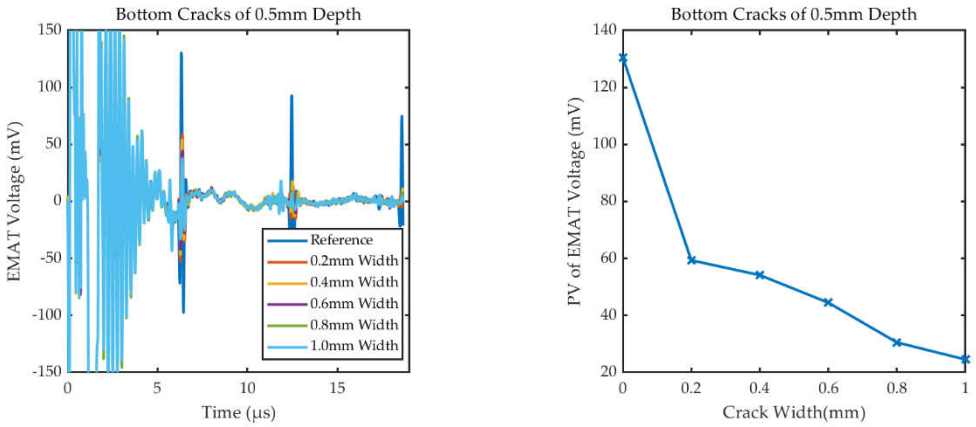

(a) **(b)**

Figure 15. Received signals by EMAT under the cracks of different widths: (**a**) Specific waveforms; (**b**) *PV*EMAT under the cracks of different widths.

4.2.2. Detection of Bottom Cracks at Different Depths

Figure 16 shows the specific waveforms and *PV*EMAT under the cracks of different depths. The thickness of testing steel sample is 20mm. The experimental results show that the signal amplitude decreases with the increase of defect depth, which is consistent with the law of the simulation results in Subsection 3.2. For the crack as small as 0.1 mm in depth, the sensor is able to recognize changes in signal amplitude. However, the defect echo is virtually unobservable when the thickness of the sample is large.

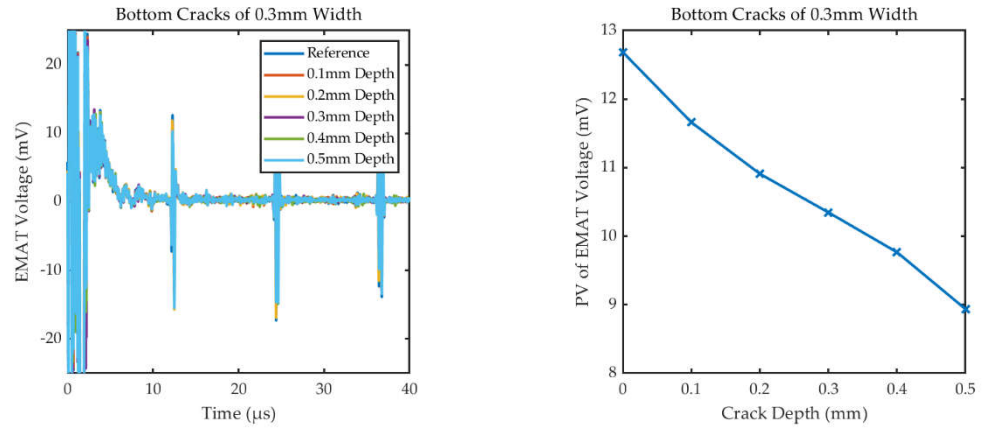

(a) **(b)**

Figure 16. Received signals of EMAT under the cracks of different depths: (**a**) Specific waveforms; (**b**) *PV*EMAT under the cracks of different depths.

Preprints.org (www.preprints.org) | NOT PEER-REVIEWED | Posted: 26 July 2024 doi:10.20944/preprints202407.2152.v1

4.2.3. Calibration Experiments

At the beginning of the experiment, the probe was placed flat on top of the steel plate for an original lift-off of 0.2 mm, then the z-axis of the motion platform was operated to elevate the probe from 0.2 mm to 2.0 mm at 0.2 mm intervals. The calibration experiments were repeated five times and the average peak value of the signals was obtained and recorded.

Figure 17 (a) shows specific waveforms of EMAT voltage under different lift-offs. The relationships and fitting results of PV_{EMAT} and $\ln(PV_{EMAT})$ to lift-offs are shown in Figure 17(b) and (c), respectively. The linearity of the fitting results between $\ln(PV_{EMAT})$ and lift-off obtained from the experiments is good, with R-square greater than 0.99, which is consistent with the simulation results in the Subsection 3.3.

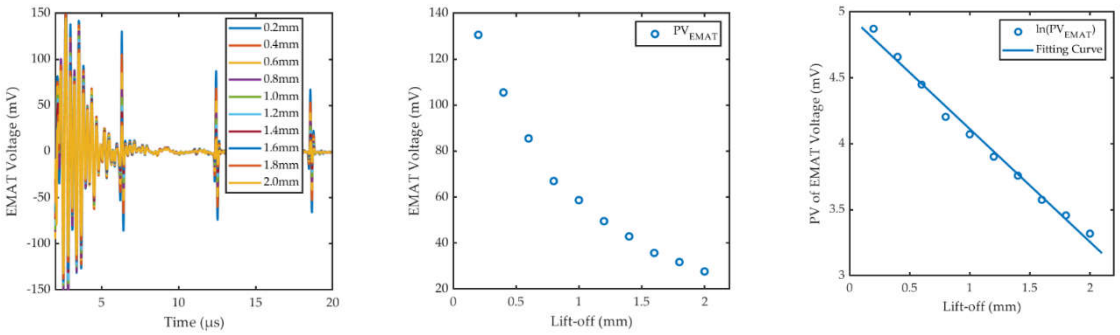

(**a**) (**b**) (**c**)

Figure 17. Received signals of EMAT coil under different lift-offs: (**a**) Specific waveforms; (**b**) PV of EMAT Voltage; (**c**) Fitting curve between $\ln(PV_{EMAT})$ and lift-offs.

Figure 18a,b show the PEC signals received by the symmetric PEC coils under different lift-offs. The fitting results of PV_{PEC} and lift-offs are shown in Figure 18 (c). The linearity of the experimentally acquired fitting curves is good, with R-square greater than 0.99, which also matches the simulation results in Subsection 3.3. The signal waveforms of the two PEC coils are similar, but the amplitudes are different, which is due to the impedance difference between the symmetric PEC coils. It can be solved by increasing circuit components to match the impedance of PEC coils, or using software for parameter adjustment to make two fitting curves consistent. In this paper, based on the existing experimental conditions, the two fitting curves obtained by calibration are used to measure the lift-offs at two points and calculate the average lift-off, which has no significant effect on the detection results.

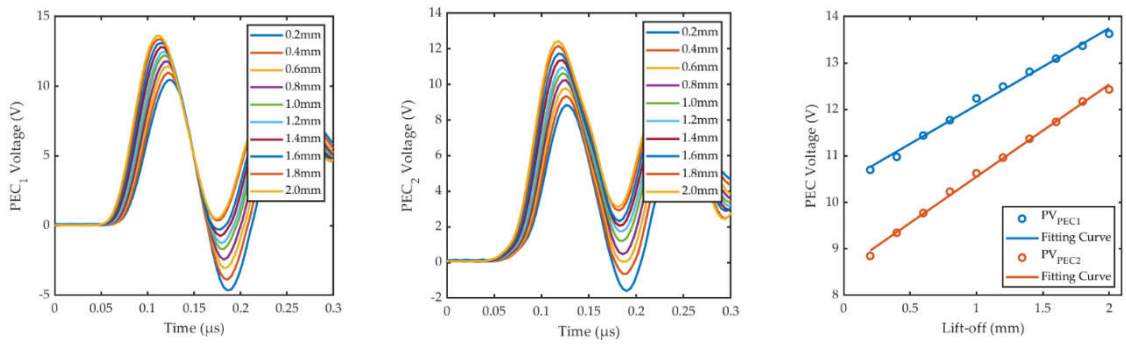

(**a**) (**b**) (**c**)

Figure 18. Received signals of symmetric PEC coils under different lift-offs: (**a**) Specific waveforms of PEC_1; (**b**) Specific waveforms of PEC_2; (**c**) Fitting curve between PV_{PEC} and lift-offs.

 doi:10.20944/preprints202407.2152.v1

The fitting functions of the signals obtained from the calibration experiments are shown in the Table 3. Based on the relationship between multiple signal features and lift-offs, we are able to further develop lift-off measurement, signal fusion and correction experiments.

Table 3. Fitting function of calibration experimental results.

Fitting Function	R-square
$\ln(PV_{EMAT}) = -0.8565 \times lo + 4.969$	0.9911
$PV_{PEC1} = 1.659 \times lo + 10.43$	0.9929
$PV_{PEC2} = 1.987 \times lo + 8.564$	0.9971

4.2.4. Comparison of Lift-Off Measurement between Symmetric PEC Coils and Single PEC Coil

To demonstrate the effectiveness of the proposed lift-off measurement method and to check its accuracy. The sheets of different sizes shown in Figure 19 were set to simulate the lift-offs caused by the vibrations of the mechanism and the non-conductive coatings on the surface of the sample during the scanning detection. The thicknesses of the sheet 1 and 2 are uniform and the measured actual thicknesses are 0.25mm and 0.504mm, respectively. The thicknesses of the sheet 3 and 4 are uneven, the measured average thicknesses are 0.702mm and 1.205mm, respectively. The sheet 1, 2, 3 and 4 were set below the probe, and the PV_{PEC1} and PV_{PEC2} were recorded by the symmetric PEC coils and the average lift-off was calculated according to the fitting function in Table 3. The results are shown in Table 4.

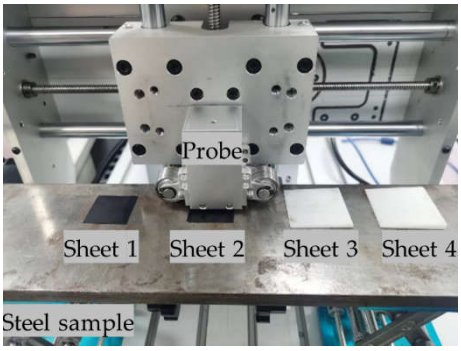

Figure 19. The setup of different sheets used to simulate lift-off fluctuation.

Table 4. Comparison of measured lift-offs and actual lift-offs.

Sheet No.	PV_{PEC1} (V)	lo_1 (mm)	PV_{PEC2} (V)	lo_2 (mm)	Average *lo* (mm)	Actual *lo* (mm)	Relative error
Sheet 1	11.138	0.427	9.444	0.443	0.435	0.250+0.2	-3.33%
Sheet 2	11.615	0.714	10.038	0.742	0.728	0.504+0.2	3.41%
Sheet 3	11.784	0.816	10.686	1.068	0.942	0.702+0.2	4.32%
Sheet 4	12.124	1.021	12.385	1.923	1.472	1.205+0.2	4.77%

From the experimental results, it can be seen that the utilization of symmetric PEC coils effectively measures the average lift-off of the probe, and the relative error is kept within ±5%. When the lift-offs on both sides of the probe are not consistent, the error of lift-off measurement is more than 20% using only the PEC_1 coil, while the design of the symmetric coil solves this problem.

4.2.5. Amplitude Correction Experiment based on Signal Fusion

Based on the signal correction and fusion method proposed in Subsection 3.3 and the fitting relationships obtained from the calibration experiments in Table 4, the signal after correcting, which is not affected by lift-off, can be represented by multiple signals fusion as,

 doi:10.20944/preprints202407.2152.v1

$$PV_{\text{Fusion}} = e^{-0.8565 \times (0.2 - \frac{(PV_{\text{PEC1}} - 10.43)/1.659 + (PV_{\text{PEC2}} - 1.987)/8.564}{2})} \times PV_{\text{EMAT}}. \quad (23)$$

In order to verify the effectiveness of the proposed real-time signal amplitude correction method based on the signal fusion, the experiments for detecting bottom cracks were carried out. We placed the sheets used in Subsection 4.2.4 under the probe to implement the detection. The PV_{EMAT} recorded by the EMAT coil and PV_{Fusion} calculated by Equation (23) are shown in Figure 20, the PV_{Original} is the reference signal of experimental results in Subsection 4.2.1. The specific experimental data for the detection and the results of signal correction are listed in Table 5.

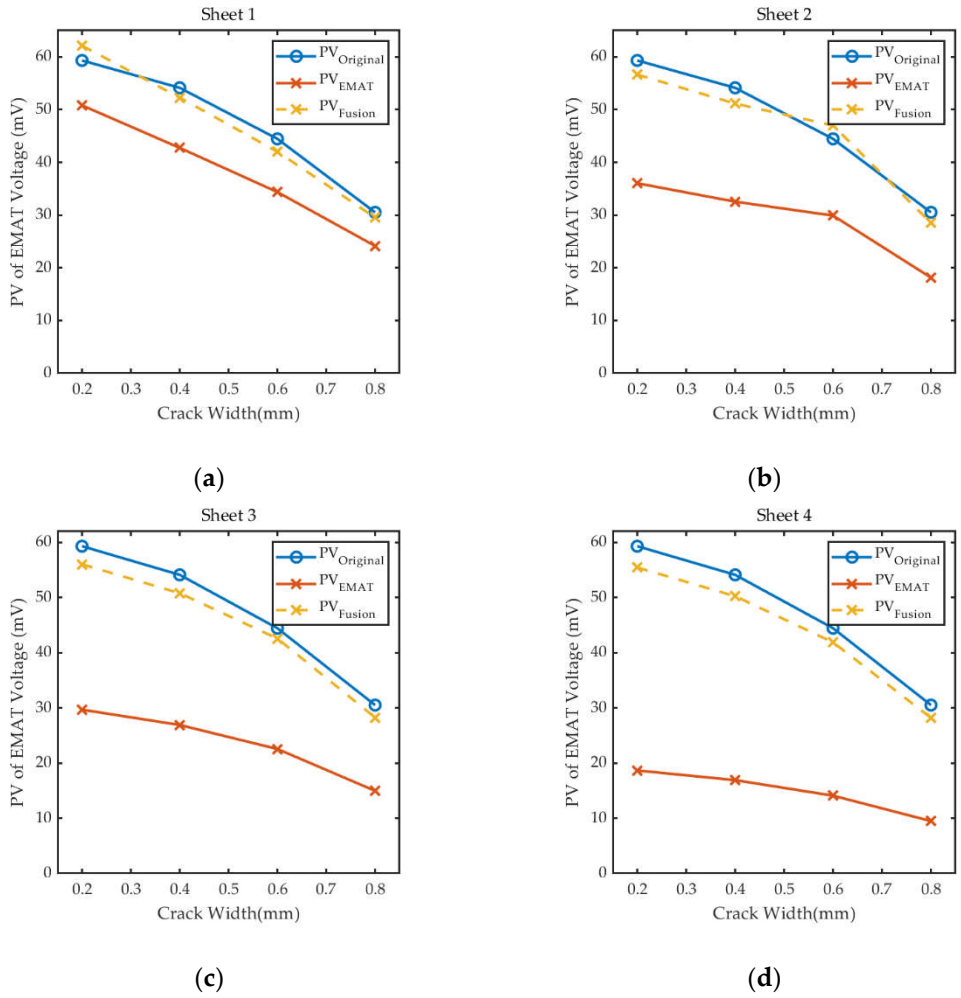

Figure 20. Correction results for crack detection signals under different lift-offs: (**a**) Lift-off caused by Sheet 1; (**b**) Lift-off caused by Sheet 2; (**c**)Lift-off caused by Sheet 3; (**d**) Lift-off caused by Sheet 4.

Table 5. Experimental data and the results of signal correction.

Sheet No.	Crack width (mm)	PV_{EMAT} (mV)	PV_{Fusion} (mV)	PV_{Original} (mV)	Relative error
Sheet 1	0.2	50.809	62.138	59.327	+4.74%
	0.4	42.747	52.278	54.135	-3.43%
	0.6	34.361	42.022	44.455	-5.47%
	0.8	24.142	29.525	30.517	-3.25%
Sheet 2	0.2	36.034	56.639	59.327	-4.53%
	0.4	32.538	51.144	54.135	-5.53%

 doi:10.20944/preprints202407.2152.v1

	0.6	29.900	46.997	44.455	+5.72%
	0.8	18.139	28.511	30.517	-6.57%
Sheet 3	0.2	29.685	56.046	59.327	-5.53%
	0.4	26.909	50.804	54.135	-6.15%
	0.6	22.556	42.586	44.455	-4.20%
	0.8	14.970	28.263	30.517	-7.39%
Sheet 4	0.2	18.660	55.470	59.327	-6.50%
	0.4	16.908	50.262	54.135	-7.15%
	0.6	14.093	41.894	44.455	-5.76%
	0.8	9.4888	28.207	30.517	-7.57%

The experimental results show that the composite detection sensor designed in this paper and the proposed real-time signal correction and fusion method are able to correct the abnormal defect detection signal, so that it is basically restored to the amplitude of the detection signal under the original lift-off. The relative error between the PV_{Fusion} and $PV_{Original}$ is less than ±8%. Thus, it can be concluded that the method can reduce the effect of lift-off on the bottom defect detection signal, ensure the consistency and accuracy of the signal in the detection process.

5. Conclusion and Future Work

5.1. Conclusion

To identify tiny bottom cracks and to ensure the accuracy and consistency of the inspection results, this paper introduces a compact EMAT-PEC composite sensor which can simultaneously detect the bottom cracks by the amplitude attenuation of the EMAT bottom echo and evaluate the posture of the probe by the symmetric PEC signals. Based on the relationships between PEC and EMAT signals and lift-offs, a signal fusion method is proposed to correct the detection signal and reduce the lift-off effect. In comparison with traditional and single EMAT, the proposed composite sensor has three main advantages:

1. The optimally designed and arranged probe is capable of exciting unidirectional shear waves with polarization direction perpendicular to the cracks, and the mode conversion occurring at the tiny crack causes the attenuation of the bottom echo amplitude. Compared with focusing on the defect echo, extracting the attenuation of the bottom echo amplitude to invert the defect size can obtain a better SNR and resolution. The experimental results prove that the probe has the ability to detect the bottom crack as small as 0.1*0.3mm;
2. The designed composite sensor can synchronously obtain the information of defect in testing sample and probe posture in real time based on EMAT echo signal and PEC signals. The whole system is supported by only one excitation source, which ensures the stability of the system and improves the energy utilization rate. The experimental results validate that symmetrically PEC coils can more accurately measure the average lift-off of the probe than a single PEC coil, with a relative error of less than ±5%.
3. The proposed signal fusion method skillfully combines the fitting relationships between the EMAT, PEC signals and the lift-offs to form a fusion signal that is not affected by lift-off, thereby effectively reducing the impact of probe fluctuation on defect detection during actual inspection. The experimental results confirm that the signal fusion method effectively corrects the effect of lift-off on the amplitude of the detection signal, and the error of the corrected signal relative to the reference signal is less than ±8%.

5.2. Future Work

It is worth noting that the amplitude of the reflected shear wave strongly depends on the relative orientation of the cracks with respect to the direction of polarization of the incident shear wave. In

 doi:10.20944/preprints202407.2152.v1

this paper, we focus on the identification of tiny bottom cracks and the correction of the signal amplitude affected by lift-off fluctuation, therefore, we ignore the effect of the crack direction, and set the scanning direction of the probe to be perpendicular to the direction of the cracks and the direction of the current in the excitation coil to be parallel to the direction of the cracks by default to obtain the best signal characteristics. In practice, the crack directions are varied, and it has been proposed to discriminate the direction and angle of the cracks by the amplitude ratio of two orthogonally arranged coils in [25]. The signal correction and fusion method proposed in our study is also of practical significance to improve the accuracy of the amplitude detection results of the two orthogonal coils.

The future work will focus on designing a self-rotating probe to detect the direction of cracks. Subsequently, we will combine it with a scanning mechanism to form the c-scan image of the tiny bottom cracks. The signal fusion method proposed in this paper can be used for image correction during probe rotation and scanning process.

Author Contributions: Conceptualization, Y.G., Z.D. and Y.K.; methodology, Y.G., Y.H., Z.D. and B.F.; validation, Y.G., W.K. and Y.S.; formal analysis, Y.G., W.K. and Z.D.; investigation, Y.G. and Y.H.; data curation, Y.G.; writing—original draft preparation, Y.G.; writing—review and editing, Y. H, K.W, Z.D., Y.S., B.F. and Y.K.; supervision, B.F. and Y.K; funding acquisition, B.F. and Y.K. All authors have read and agreed to the published version of the manuscript.

Funding: This research was funded by National Key Natural Science Foundation of China (No. 52130504) and National Natural Science Foundation of China (No. 52105551).

Conflicts of Interest: The authors declare no conflicts of interest.

References

1. Yao, Y.; Tung, S.-T.E.; Glisic, B. Crack Detection and Characterization Techniques-An Overview. *Structural Control and Health Monitoring* **2014**, *21*, 1387–1413, doi:10.1002/stc.1655.
2. Vanaei, H.R.; Eslami, A.; Egbewande, A. A Review on Pipeline Corrosion, in-Line Inspection (ILI), and Corrosion Growth Rate Models. *International Journal of Pressure Vessels and Piping* **2017**, *149*, 43–54, doi:10.1016/j.ijpvp.2016.11.007.
3. Kong, Y.; Bennett, C.J.; Hyde, C.J. A Review of Non-Destructive Testing Techniques for the in-Situ Investigation of Fretting Fatigue Cracks. *Materials & Design* **2020**, *196*, 109093, doi:10.1016/j.matdes.2020.109093.
4. Wu, J.; Yang, Y.; Li, E.; Deng, Z.; Kang, Y.; Tang, C.; Sunny, A.I. A High-Sensitivity MFL Method for Tiny Cracks in Bearing Rings. *IEEE Trans. Magn.* **2018**, *54*, 1–8, doi:10.1109/TMAG.2018.2810199.
5. Ravan, M.; Amineh, R.K.; Koziel, S.; Nikolova, N.K.; Reilly, J.P. Estimation of Multiple Surface Cracks Parameters Using MFL Testing. In Proceedings of the 2010 URSI International Symposium on Electromagnetic Theory; IEEE: Berlin, Germany, August 2010; pp. 891–894.
6. Ege, Y.; Bicakcı, S.; Gunes, H.; Citak, H.; Coramik, M. An Application of BRANN and MFL Methods: Determining Crack Type and Physical Properties on M5 Steel Sheets. *Measurement* **2019**, *138*, 545–556, doi:10.1016/j.measurement.2019.02.064.
7. Hamia, R.; Cordier, C.; Dolabdjian, C. Eddy-Current Non-Destructive Testing System for the Determination of Crack Orientation. *NDT & E International* **2014**, *61*, 24–28, doi:10.1016/j.ndteint.2013.09.005.
8. Dai, L.; Feng, H.; Wang, T.; Xuan, W.; Liang, Z.; Yang, X. Pipe Crack Recognition Based on Eddy Current NDT and 2D Impedance Characteristics. *Applied Sciences* **2019**, *9*, 689, doi:10.3390/app9040689.
9. Yuan, F.; Yu, Y.; Li, L.; Tian, G. Investigation of DC Electromagnetic-Based Motion Induced Eddy Current on NDT for Crack Detection. *IEEE Sensors J.* **2021**, *21*, 7449–7457, doi:10.1109/JSEN.2021.3049551.
10. Kim, G.; Seo, M.-K.; Kim, Y.-I.; Kwon, S.; Kim, K.-B. Development of Phased Array Ultrasonic System for Detecting Rail Cracks. *Sensors and Actuators A: Physical* **2020**, *311*, 112086, doi:10.1016/j.sna.2020.112086.
11. Drinkwater, B.W.; Wilcox, P.D. Ultrasonic Arrays for Non-Destructive Evaluation: A Review. *NDT & E International* **2006**, *39*, 525–541, doi:10.1016/j.ndteint.2006.03.006.
12. Wang, K.; Song, Y.; Kang, Y.; Guo, Y.; Ma, H.; Wu, S.; Yang, J. Ultrasonic Detection Method Based on Flexible Capillary Water Column Arrays Coupling. *Ultrasonics* **2024**, *139*, 107276, doi:10.1016/j.ultras.2024.107276.
13. Zhang, J.; Liu, M.; Jia, X.; Gao, R. Numerical Study and Optimal Design of the Butterfly Coil EMAT for Signal Amplitude Enhancement. *Sensors* **2022**, *22*, 4985, doi:10.3390/s22134985.

14. Wang, S.; Huang, S.; Zhang, Y.; Zhao, W. Multiphysics Modeling of a Lorentz Force-Based Meander Coil Electromagnetic Acoustic Transducer via Steady-State and Transient Analyses. *IEEE Sensors J.* **2016**, *16*, 6641–6651, doi:10.1109/JSEN.2016.2587620.
15. Lunn, N.; Dixon, S.; Potter, M.D.G. High Temperature EMAT Design for Scanning or Fixed Point Operation on Magnetite Coated Steel. *NDT & E International* **2017**, *89*, 74–80, doi:10.1016/j.ndteint.2017.04.001.
16. Gao, H.; Ali, S.; Lopez, B. Efficient Detection of Delamination in Multilayered Structures Using Ultrasonic Guided Wave EMATs. *NDT & E International* **2010**, *43*, 316–322, doi:10.1016/j.ndteint.2010.03.004.
17. Liu, T.; Pei, C.; Cai, R.; Li, Y.; Chen, Z. A Flexible and Noncontact Guided-Wave Transducer Based on Coils-Only EMAT for Pipe Inspection. *Sensors and Actuators A: Physical* **2020**, *314*, 112213, doi:10.1016/j.sna.2020.112213.
18. Pei, C.; Liu, T.; Chen, H.; Chen, Z. Inspection of Delamination Defect in First Wall with a Flexible EMAT-Scanning System. *Fusion Engineering and Design* **2018**, *136*, 549–553, doi:10.1016/j.fusengdes.2018.03.018.
19. Tu, J.; Zhong, Z.; Song, X.; Zhang, X.; Deng, Z.; Liu, M. An External through Type RA-EMAT for Steel Pipe Inspection. *Sensors and Actuators A: Physical* **2021**, *331*, 113053, doi:10.1016/j.sna.2021.113053.
20. Felice, M.V.; Fan, Z. Sizing of Flaws Using Ultrasonic Bulk Wave Testing: A Review. *Ultrasonics* **2018**, *88*, 26–42, doi:10.1016/j.ultras.2018.03.003.
21. Sun, H.; Urayama, R.; Uchimoto, T.; Takagi, T.; Hashimoto, M. Small Electromagnetic Acoustic Transducer with an Enhanced Unique Magnet Configuration. *NDT & E International* **2020**, *110*, 102205, doi:10.1016/j.ndteint.2019.102205.
22. Maiyi, Z.; Renwen, C.; Yufeng, Z. Design and Optimization of Electromagnetic Ultrasonic Body Wave Probe Based on Halbach Structure. *39*.
23. Sun, H.; Huang, S.; Wang, Q.; Wang, S.; Zhao, W. Orthogonal Optimal Design Method for Point-Focusing EMAT Considering Focal Area Dimensions. *Sensors and Actuators A: Physical* **2020**, *312*, 112109, doi:10.1016/j.sna.2020.112109.
24. Jia, X.; Ouyang, Q.; Zhang, X. An Improved Design of the Spiral-Coil EMAT for Enhancing the Signal Amplitude. *Sensors* **2017**, *17*, 1106, doi:10.3390/s17051106.
25. Parra-Raad, J.; Khalili, P.; Cegla, F. Shear Waves with Orthogonal Polarisations for Thickness Measurement and Crack Detection Using EMATs. *NDT & E International* **2020**, *111*, 102212, doi:10.1016/j.ndteint.2019.102212.
26. Feng, J.; Lu, S.; Liu, J.; Li, F. A Sensor Liftoff Modification Method of Magnetic Flux Leakage Signal for Defect Profile Estimation. *IEEE Trans. Magn.* **2017**, *53*, 1–13, doi:10.1109/TMAG.2017.2690628.
27. Wang, S.; Hu, Y.; Duan, Z.; Jiang, C.; Kang, Y.; Feng, B. AC Magnetic Flux Leakage Testing With Real-Time Liftoff Compensation Using Double Layer Parallel-Cable Probe. *IEEE Trans. Instrum. Meas.* **2024**, *73*, 1–9, doi:10.1109/TIM.2024.3351230.
28. Xiang, L.; Dixon, S.; Thring, C.B.; Li, Z.; Edwards, R.S. Lift-off Performance of Electromagnetic Acoustic Transducers (EMATs) for Surface Acoustic Wave Generation. *NDT & E International* **2022**, *126*, 102576, doi:10.1016/j.ndteint.2021.102576.
29. Feng, B.; Xie, S.; Xie, L.; Deng, K.; Wang, S.; Kang, Y. Analysis of the Lift-Off Effect in Motion-Induced Eddy Current Testing Based on Semi-Analytical Model. *IEEE Trans. Instrum. Meas.* **2024**, *73*, 1–8, doi:10.1109/TIM.2023.3347805.
30. Hu, Y.; Wang, S.; Duan, Z.; Gao, Y. A Method for Compensation of Permanent Magnetic Field Perturbation (PMFP) Testing Signal Based on Lift-off Measurement. *Meas. Sci. Technol.* **2023**, *34*, 125129, doi:10.1088/1361-6501/acf1bd.
31. Duan, Z.; Kang, Y.; Chen, Y.; Wan, Z.; Wang, S. Reduction of Lift-off Effect in Pulsed Eddy Current Testing for Surface Hardness Classification of Ferromagnetic Steel. *Measurement* **2022**, *205*, 112191, doi:10.1016/j.measurement.2022.112191.
32. Duan, Z.; Guo, Y.; Cheng, S.; Kang, Y.; Hu, Y.; Chen, Y.; Li, Y.; Feng, B. A Lift-off Measurement and Compensation Method Based on a Comprehensive EMAT-PEC Probe. *Sensors and Actuators A: Physical* **2024**, *372*, 115319, doi:10.1016/j.sna.2024.115319.
33. Wang, S.; Li, Z.; Kang, L.; Hu, X.; Zhang, X. Modeling and Comparison of Three Bulk Wave EMATs. In Proceedings of the IECON 2011 - 37th Annual Conference of the IEEE Industrial Electronics Society; IEEE: Melbourne, Vic, Australia, November 2011; pp. 2645–2650.
34. Hirao, M.; Ogi, H. *Electromagnetic Acoustic Transducers: Noncontacting Ultrasonic Measurements Using EMATs*; Springer Series in Measurement Science and Technology; Springer Japan: Tokyo, 2017; ISBN 978-4-431-56034-0.

 doi:10.20944/preprints202407.2152.v1

35. Harker, A.H. Numerical Modelling of the Scattering of Elastic Waves in Plates. *J Nondestruct Eval* **1984**, *4*, 89–106, doi:10.1007/BF00566400.
36. MacLauchlan, D.; Clark, S.; Cox, B.; Doyle, T.; Grimmett, B.; Hancock, J.; Hour, K.; Rutherford, C. Recent Advancements in the appplication of EMATs to NDE. In Proceedings of the Sixteenth World Conf. NDT, 2004, pp. 1154-1161.